Fourier and wavelet analyses of TOPEX/Poseidon-derived sea level anomaly over the South China Sea: A contribution to the South China Sea Monsoon Experiment

Cheinway Hwang and Sung-An Chen
Department of Civil Engineering, National Chiao Tung University, Hsinchu, Taiwan

Abstract. We processed 5.6 years of TOPEX/Poseidon altimeter data and obtained time series of sea level anomaly (SLA) over the South China Sea (SCS). Fourier analysis shows that sea level variability of the SCS contains major components with periods larger than 180 days and is dominated by the annual and semiannual components. Tidal aliasing creates 30-180 day components that can be misinterpreted as wind-induced variabilities. Continuous and multiresolution wavelet analyses show that the SLA of the SCS has monthly to interannual components of time-varying amplitudes, and the regional slope of SLA is 8.9 mm yr^{-1}, which may be caused by the decadal climate change. Coherences of SLA with wind stress anomalies (WSA) and sea surface temperature anomalies (STA) are significant at the annual and semi-annual components. At periods of 2-5 years the wavelet coefficients of SLA, WSA, and STA have the same pattern, but WSA leads SLA, and STA follows SLA. The zero crossing of SLA in spring is highly correlated with the onset of the summer monsoon. The interannual variability of SLA is correlated with El Niño-Southern Oscillation, and most important is that when the El Niño-like wavelet coefficients of SLA over the warm pool northeast of Australia or the SCS change curvature from negative to positive, an El Niño is likely to develop. This is a contribution to the South China Sea Monsoon Experiment (SCSMEX).

1. Introduction

The South China Sea (SCS) is the largest marginal sea in the western Pacific with a total area of 2,590,000 km^2. Figure 1 shows the countries, waters, major islands and bottom features, and major depth contours around the SCS. The South China Sea Monsoon Experiment (SCSMEX) is an international project to study the monsoons over the SCS. The participating countries include most countries in east Asia and southeast Asia, Australia, and the United States. Its purpose is to "better understand the key physical processes in the onset, maintenance, and variability of the monsoon over southeast Asia and southern China" [*Lau*, 1997, p. 599]. We have joined SCSMEX to investigate the characteristics of sea level variability over the SCS derived from the TOPEX/Poseidon (T/P) altimeter. We will perform Fourier and wavelet analyses of the T/P-derived sea level time series. Compared to Fourier analysis, wavelet analysis is a recently developed tool that is best suited for analyzing phenomena with time-varying frequencies and amplitudes. An extensive body of literature associated with wavelet analysis has been developed over the past decade. The lectures by *Daubechies* [1992] provide readers with both an introductory and an in-depth understanding of wavelets. A practical guide to wavelet analysis is given by in *Torrence and Compo* [1998]. A collection of applications of wavelets in geophysics and oceanography is given by in *Foufoula-Georgiou and Kumar* [1994]. Moreover, we will compute the frequency response functions and coherence functions [*Bendat and Piersol*, 1993] between sea level, wind, and sea surface temperature over the SCS to see the degrees of interaction among these signals. The relationships of sea level variability to

the summer and winter monsoons over the SCS and to El Niño-Southern Oscillation (ENSO) will also be studied.

2. Sea Level Anomaly From TOPEX/Poseidon

T/P is a satellite altimeter mission specifically designed to measure the height of the sea level with a repeat period of 9.9156 days. We used the T/P Version C Geophysical Data Records (GDRs) from Archiving, Validation, Interpretation of Satellite Oceanographic Data (AVISO) [1996] to generate corrected sea surface heights (SSHs) from cycle 10 (December 26, 1992) to cycle 219 (August 29, 1998). The first nine cycles were not used because of a pointing problem [*Fu et al.*, 1994]. The orbit we used in the T/P GDRs is based on the Joint Gravity Model 3 (JGM3) gravity field [*Tapley et al.*, 1996] and has an accuracy of about 4 cm. The dry tropospheric and inverse barometric corrections were based on the European Centre for Medium Range Weather Forecasts (ECMWF) model. The wet tropospheric corrections were directly taken from the TOPEX Microwave Radiometer (TMR) measurements. For the ionospheric correction, TOPEX uses its dual frequency measurements and Poseidon is based on the model of Doppler orbitography and radiopositioning integrated by satellite (DORIS). The CSR3.0 ocean tide model [*Eanes and Bettadpur*, 1995] was used to detide the data. In particular, an oscillator drift correction has been applied to the TOPEX range measurements [AVISO, 1996]. To produce SLAs for the subsequent analyses, we first formed stacked along-track SSHs by averaging the point SSHs from the 210 T/P cycles. When averaging, the gradient of a geoid computed from the Earth Gravitational Model 1996 (EGM96) to harmonic degree 360 [*Lemoine et al.*, 1998] was used to reduce point SSHs to the nominal ground tracks selected to correspond with the tracks of cycle 92 for this study. A point SLA was computed as

$$\Delta h = h - \bar{h}, \tag{1}$$
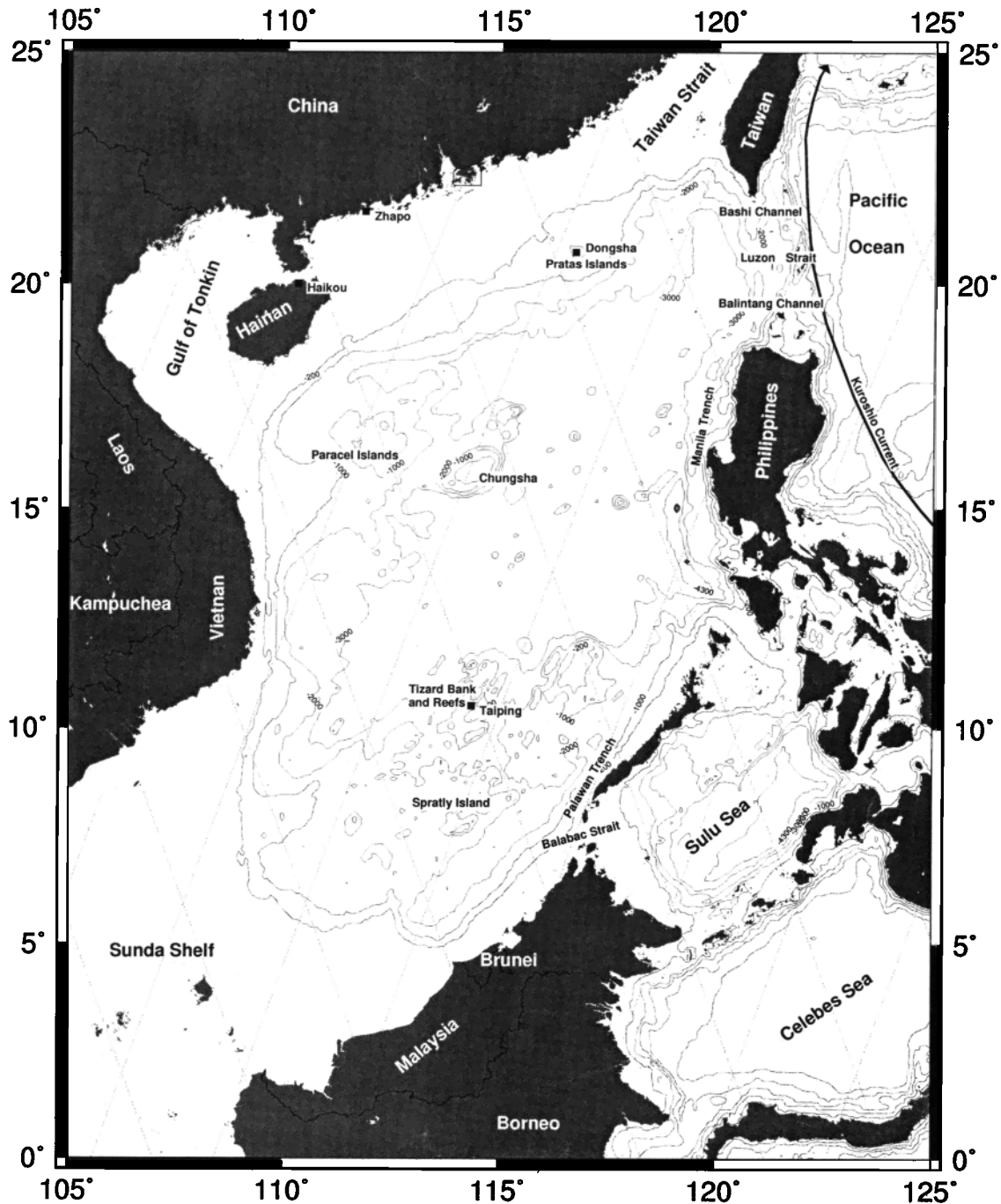
Figure 1. The South China Sea and its surrounding countries and waters. Also given are selected depth contours (solid lines), the ground tracks of TOPEX/Poseidon (dots), major bottom features, and islands. Squares indicate tide gauge stations.

where h and $\bar{h}$ are point and averaged SSH, respectively. An area-averaged SLA over a given area is the simple mean of all point SLAs in the area, and the associated time is the central time of the T/P cycle. In computing the simple mean we rejected outlier SLAs using Pope's [1976] τ - test. An outlier point SLA satisfies

$$\tau = \frac{|v_i|}{\hat{\sigma}_i} > \tau_{\alpha;1,n-2} \quad , \tag{2}$$

where v_i and $\hat{\sigma}_i$ are the residual of a SLA (observation minus area mean) and the residual's a posterior standard error,

respectively, α is the confidence level, which is 95% in this paper, n is the number of point SLAs, and $\tau_{\alpha,1,n-2}$ is the critical τ value with degrees of freedom of 1 and n -2. Outlier rejection was performed iteratively until no outlier was found, and the final area-averaged SLA was computed from the "clean" set of point SLAs. On the basis of Figure 1, SCS depths range from less than 200 m over the continental shelf to 6000 m at the center of the basin and at the Manila Trench. From numerical models [*Shaw and Chao*, 1994] and drifter data [*Hu*, 1998] the SCS has two distinct circulation systems that are roughly separated at 14.5° N. Moreover,
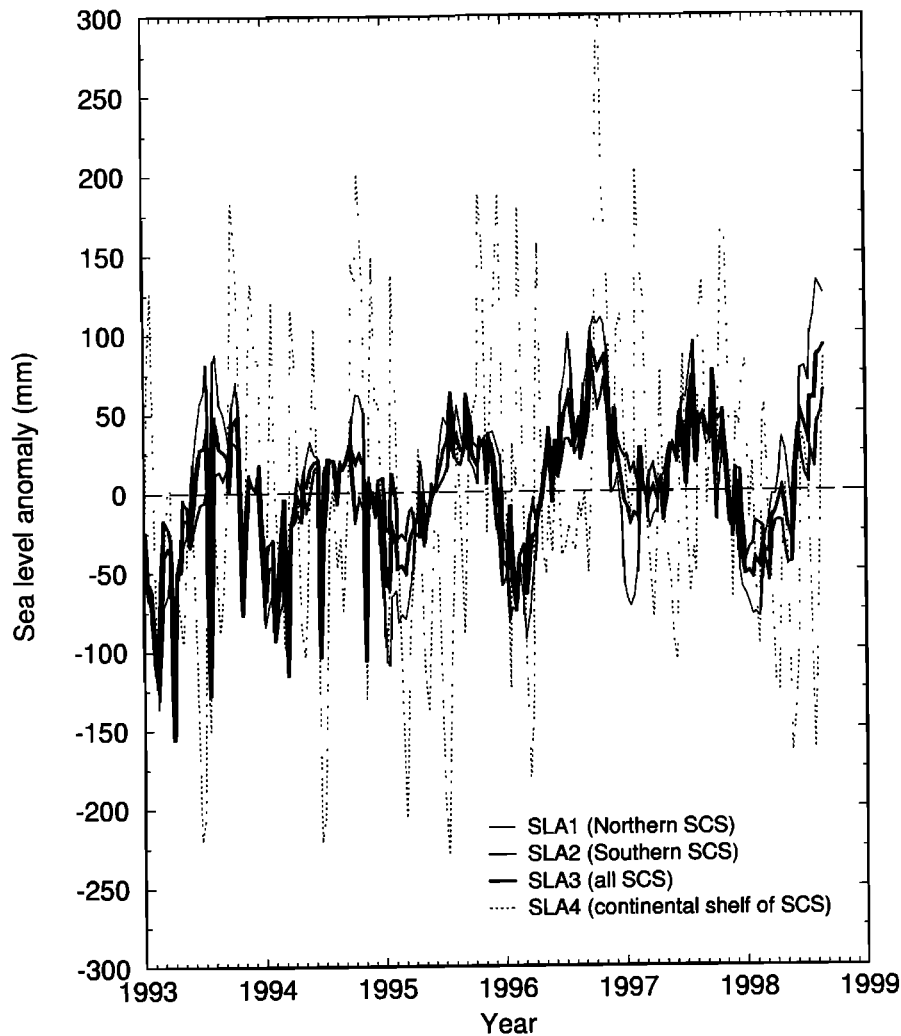
Figure 2. Time series of SLA in four areas of the SCS.

altimeter-observed SSHs over shallow water will have larger errors than those over the deep ocean. To see the spatial characteristics of the SCS sea level, we computed SLA time series in four subareas of the SCS: The first one (SLA1) is over the deep ocean (depths > 200 m) between 14.5° and 22°N , the second (SLA2) is over the deep ocean between 5° and 14.5°N , the third (SLA3) is over the deep ocean between 5° and 22°N (this area combines the first and the second areas), and the last (SLA4) is over the continental shelf (defined as the area with depths <200 m) and between 14.5° and 22°N . Figure 2 shows the four SLA time series. Note that the time series in Figure 2 and other figures in this paper have the beginning of each year (January 1) labeled. In general, SLA1, SLA2, and SLA3, which are over the deep ocean, agree very well with each other but are significantly different from SLA4. SLA3 behaves basically as the average of SLA1 and SLA2.

Table 1 shows the statistics in generating the four SLA time series. The large percentage of rejected SLAs in SLA4 is due to the large ocean tide model error, distortions of altimeter footprints, and wind-driven events. Figure 3 shows the standard errors of the area means in the four SLA time series. The standard error of an area mean, σ_m, is computed by

$$\sigma_m = \sqrt{(\sum_{i=1}^{n} v_i^2)/n(n-1)} \ , \tag{3}$$

where v_i and n are defined in (2). By this definition a SLA standard error will be affected by the variability of the sea surface under study. It appears that the SLA4 error is not random and has periodic components arising from ocean tide model errors. A

Table 1. Statistics of Area-Averaged SLA over the SCS

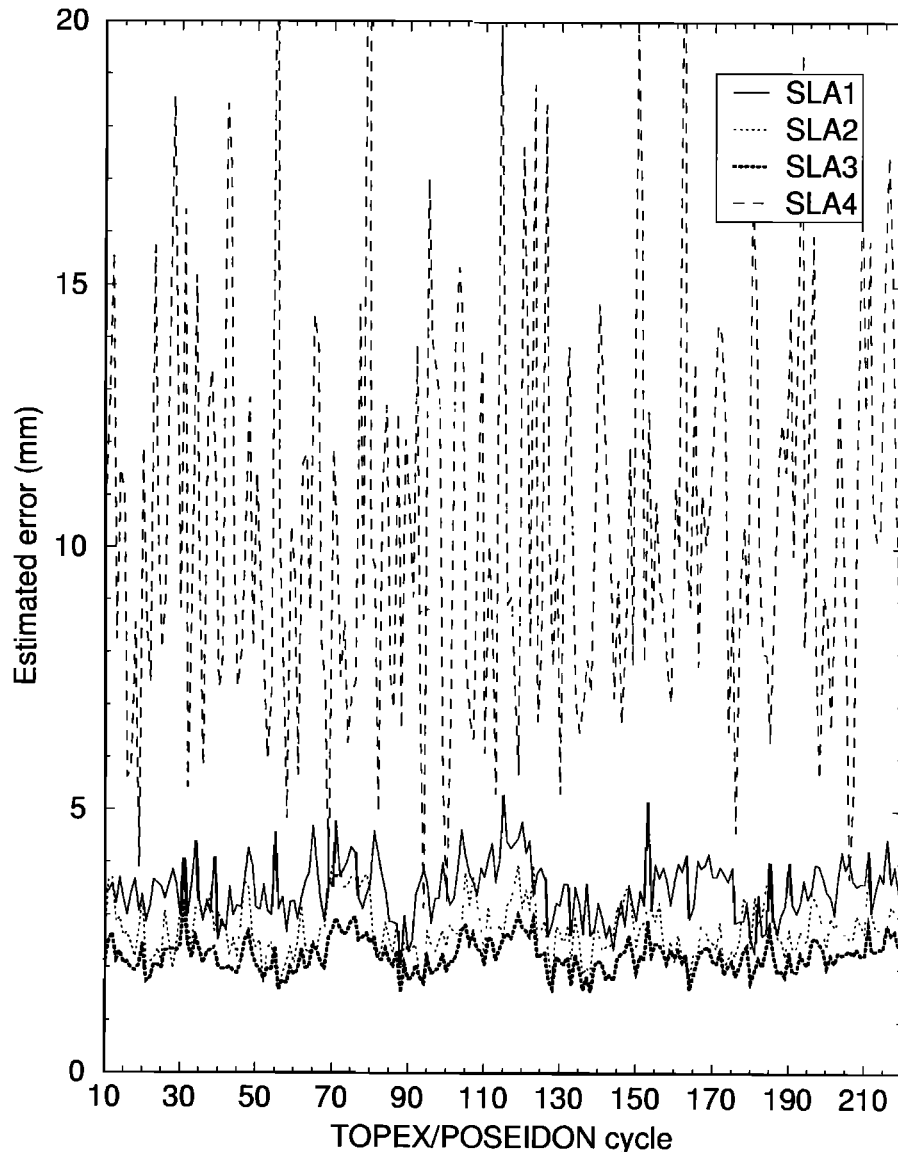|	North	South	All	Continental Shelf
Number of selected points	727	997	1726	132
Percentage of rejected points, %	0.76	1.66	1.15	3.73
Mean standard error, mm	3.49	2.75	2.24	10.53

Figure 3. Estimated errors (1 standard deviation) of the area-averaged SLA in four areas of the SCS.

spectral analysis shows that the spectrum of the SLA4 error is almost "flat," except at two distinct, large components: the largest component has a period of 59 days and an amplitude of 1.2 mm, and the next one has a period of 27 days and an amplitude of 0.8 mm. These two components have to do with the T/P tidal aliasing discussed below. In addition, the SLA2 error is smaller than the SLA1 error because SLA2 uses more data points than SLA1, and the northern SCS has a much larger sea surface variability than the southern SCS [*Hwang and Chen*, 2000].

3. Fourier Spectra of Sea Level Anomaly

3.1. Periodograms

To see the overall characteristics of the sea level variability over the SCS in the frequency domain, we performed Fourier transforms to obtain periodograms of SLA1, SLA2, SLA3, and SLA4 (Figure 4). Table 2 shows the amplitudes and periods of the first 10 largest components of the four SLA series. All four SLA series have strong components with a period of 345 days, which correspond to the annual component. The annual component of

SLA1 is much larger than that of SLA2 because of the higher latitude of the northern SCS, which is more sensitive to the seasonal variation in solar insulation than the southern SCS. Figure 5 shows the filtered SLA time series that were computed using a Gaussian filter with a wavelength of 1 year; see *Wessel and Smith* [1995] for the definition of the Gaussian filter and its wavelength. Clearly, the annual components over the northern, southern, and continental shelf parts of the SCS have summer peaks at different times of the year. Comparing the phases of the annual components, we find that summer peaks for SLA1 lead those of SLA2 by 21 days and SLA4 by 76 days. In the four SLA time series, there are two strong interannual components with periods of 1036 and 2072 days, which will be investigated in connection to ENSO. Again, in all aspects, SLA3 behaves essentially as the average of SLA1 and SLA2.

3.2. Tidal Aliasing in TOPEX/Poseidon

SLA4, being over the continental shelf, has a distinct Fourier spectrum compared to those of SLA1-SLA3. SLA4 has strong components with periods of 61 and 63 days (Table 2), which are
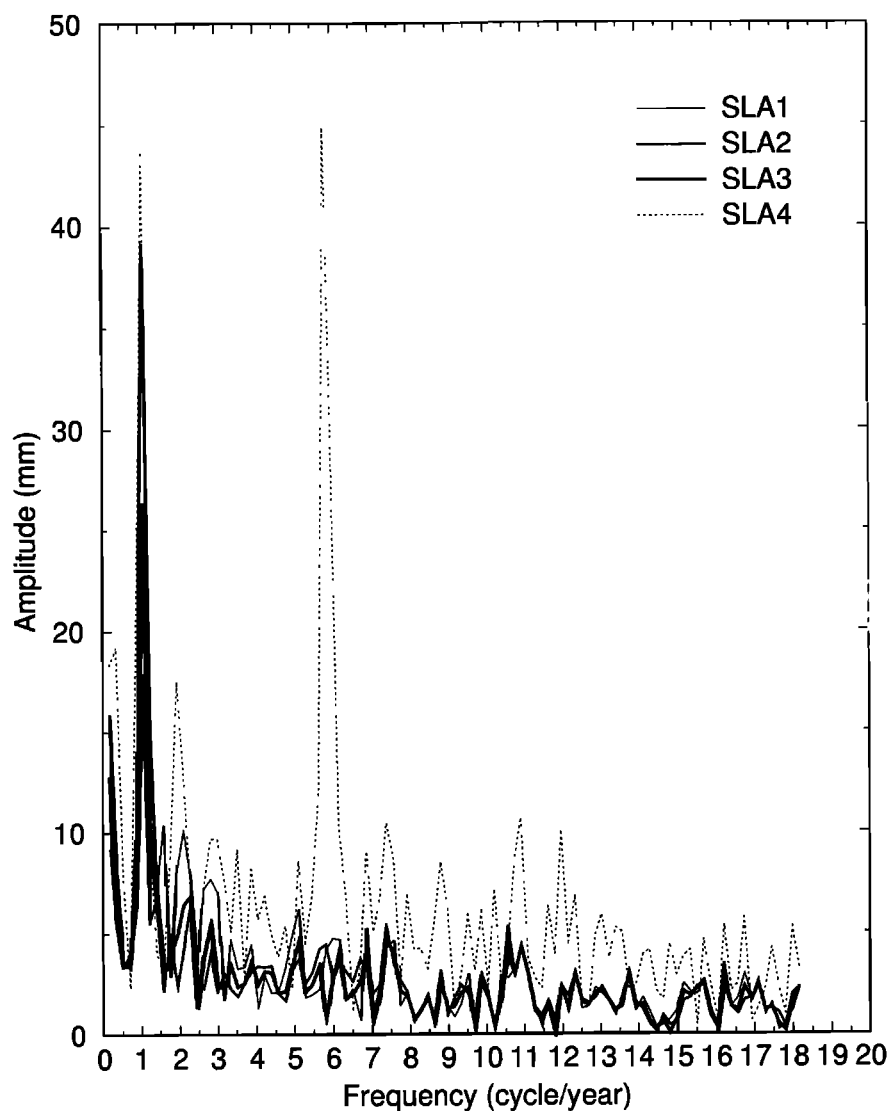
Figure 4. Periodograms of SLA time series in four areas of the SCS.

Table 2. Periods and Amplitudes of the 10 Leading Components of the Four SLA Time Series Over the SCS
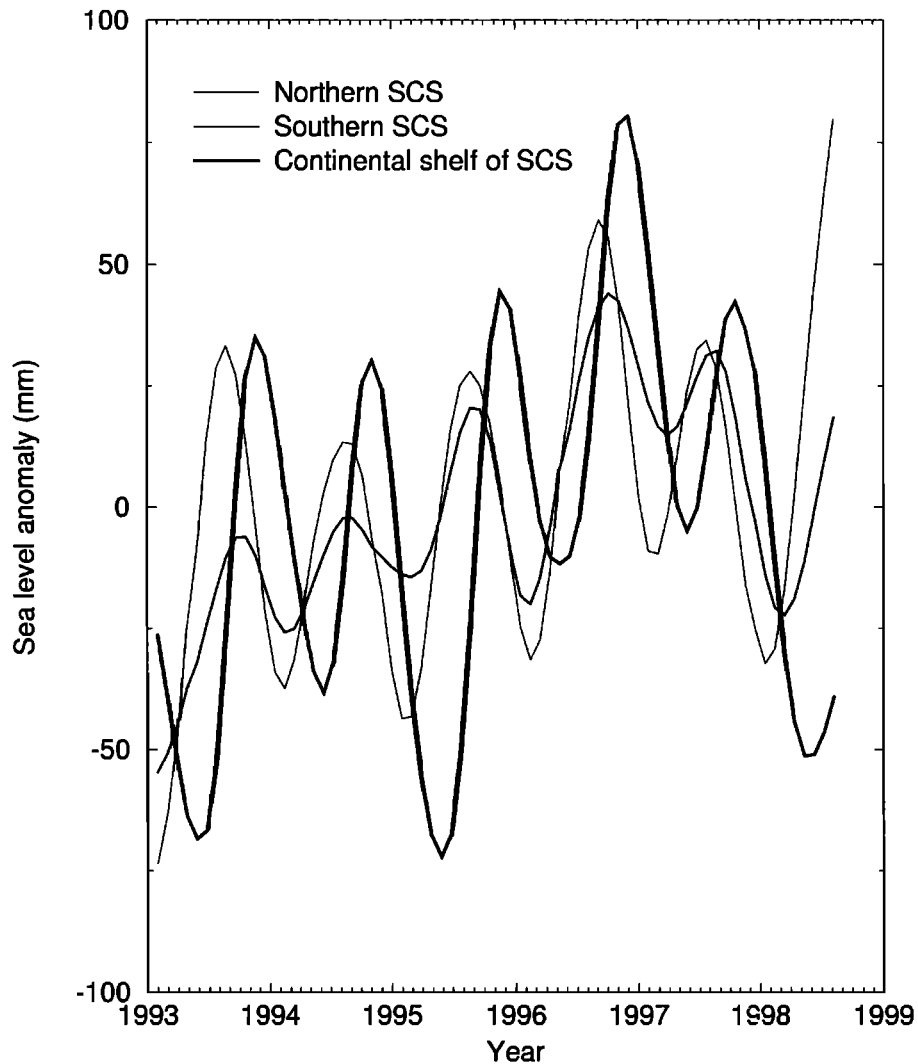
North		South		All		Continental shelf	
(Period, days	Amplitude, mm)	(Period, days	Amplitude, mm)	(Period, days	Amplitude, mm)	(Period, days	Amplitude, mm)
345	39	345	18	345	26	63	45
296	15	2072	16	2072	13	345	44
230	10	1036	8	296	10	61	28
173	10	259	7	414	8	1036	19
414	10	414	7	159	7	414	19
2072	9	159	6	259	7	2072	18
188	8	296	6	173	6	188	18
159	8	49	5	1036	6	173	13
130	8	35	5	130	5	65	12
138	7	207	5	188	5	33	11
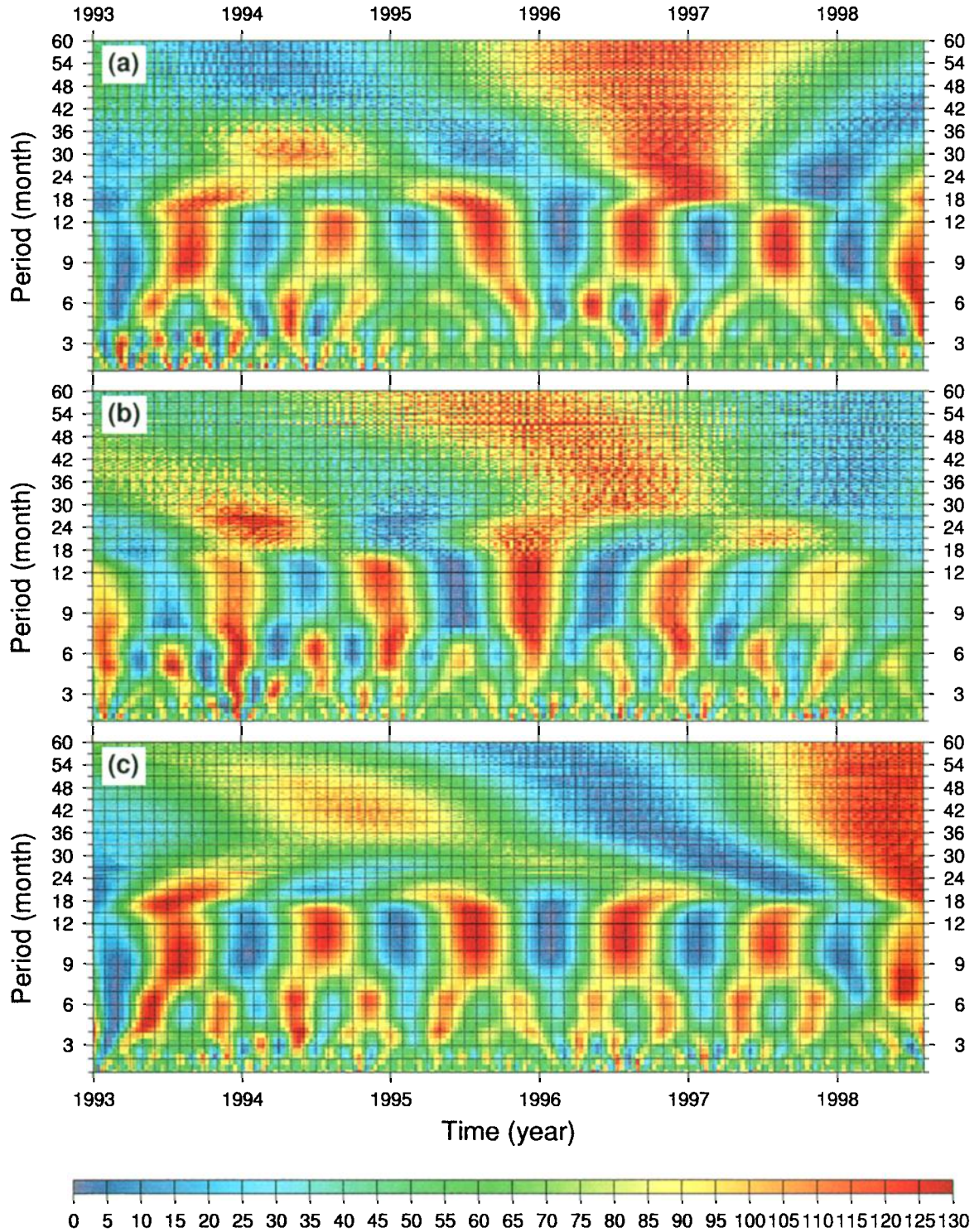
Plate 1. Wavelet coefficients of (a) SLA, (b) wind stress anomaly, and (c) sea surface temperature anomaly over the SCS. The period of a wavelet coefficient is in the sense of Fourier analysis. The unit of coefficients is arbitrary. A coefficient of 130 means that the corresponding wavelet has the maximum similarity with the signal, $f(t)$; a coefficient of 0 means that the wavelet has the maximum similarity with $-f(t)$; a coefficient of 65 implies the least similarity between the wavelet and $f(t)$.
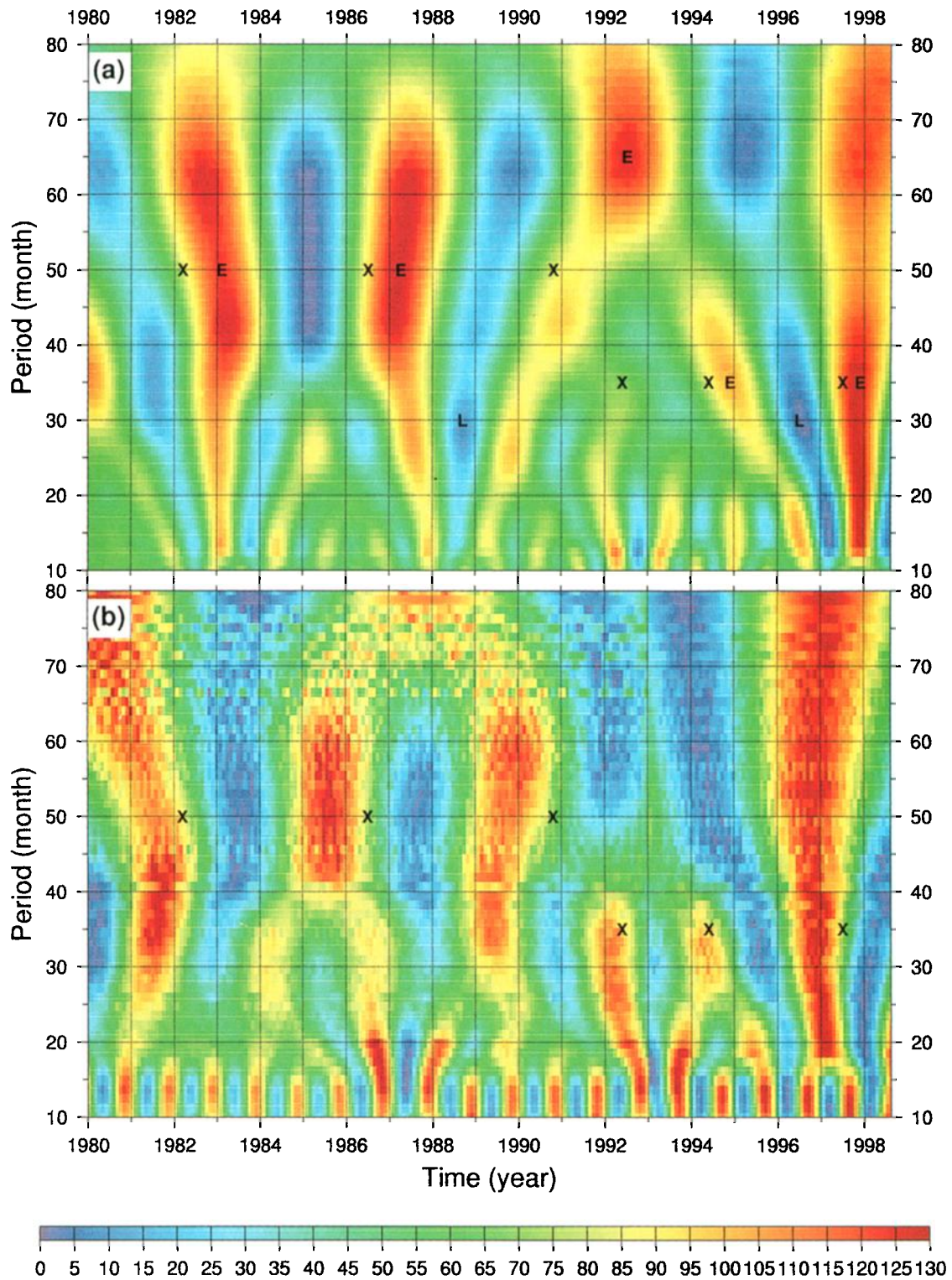
Plate 2. Wavelet coefficients of (a) NINO3 SST and (b) extended SLA over the SCS. Period and interpretation of wavelet coefficients are the same as those given in Plate 1. The centers of "E" and "L" mark the locations of the peaks of El Niño and La Nina, and the center of "X" marks the location where the El Niño-like wavelet coefficients of SLA change curvature from negative to positive.

Figure 5. Time series of smoothed SLA showing the annual variation of sea level in the northern, southern, and continental shelf of SCS.

relatively weak in the other SLA series. The amplitudes of the components with periods of 173 and 188 days in SLA4 reach 1-2 cm and are considered large compared to the same components in the others. These components may well be aliased tidal signals arising from the error of the CSR3.0 tide model we used in generating SLAs. Table 3 lists the tidal aliasing periods of 11 major ocean tides for T/P, which were computed using [*Parke et al.*, 1987; *Schlax and Chelton*, 1994]

$$T(f) = \frac{p}{fp - [fp + 0.5]} , \qquad (4)$$

where f is the tidal frequency, $p = 9.9156$ days is the T/P repeat period, and $[fp + 0.5]$ is the integer part of (fp +0.5). For T/P the aliasing periods of the major ocean tides range from 28 to 183 days and can be mistakenly associated with monthly, intraseasonal, and semiannual sea level variability generated by wind and other forcings. Table 4 shows the amplitudes and phases of the CSR3.0 tide model errors at Haikuo, Dongsha, and Taiping tide gauge stations, whose locations are given in Figure 1. To determine the CSR3.0 model error at a tide gauge station, we first subtracted the CSR3.0 modeled values from the measured values to get the errors. The measured values are given at 1 hour intervals, and the record

length we used is 1 year. Then the phases and the amplitudes of the errors at given tidal frequencies were computed by a least squares harmonic analysis. In general, CSR3.0 has the least error at Dongsha, which is surrounded by deep waters. At Haikuo the largest error occurs at K_1, while at Taiping and Dongsha the largest errors occur at M_2. Although Haikuo is located on the continental shelf and has the largest error at K_1, the strongest components in SLA4 are those with periods of 60-62 days, which we believe are due to aliased M_2 and S_2. Moreover, SLA1 has a relatively strong 173 day component, which becomes smaller in SLA3. SLA3, being the average of SLA1 and SLA2, contains less tidal aliasing effect because it has no significant components with periods close to the tidal aliasing periods. In practice, if the phase of an aliased tide is spatially smooth, then the tidal aliasing effect may be reduced by averaging SLAs over an area larger than the wavelength of this aliased tide. Formulae for computing the wavelengths of aliased tides are given by *Schlax and Chelton* [1994]. For example, the wavelength of the aliased M_2 for T/P is 9°. The widths of the northern SCS and the southern SCS are just about the wavelength of the aliased M_2, and hence SLA1 and SLA2 may marginally escape the contamination of the aliased M_2 tide. Because the whole SCS extends more than 9°, SLA3 is less likely to be affected by the aliased M_2 tide. However, the width of

Table 3. Tidal Aliasing Periods of TOPEX/Poseidon for 11 Major Ocean Tides

Tide	Aliasing Period, days
M_2	62
S_2	59
N_2	50
K_2	87
O_1	46
K_1	173
Q_1	69
Mm	28
Mf	36
Ssa	183

the continental shelf of the SCS is $< 9°$, hence, along with the fact that the M_2 error and its phase variation are large, SLA4 contains a strong component with period equal to the aliasing period of M_2. For comparison, in Figure 6 we show the periodograms of SLA4, as well as SLA series over the Taiwan Strait, the East China Sea, and the Yellow Sea, which are all located on the continental shelf of east Asia. All the SLA series in Figure 6 contain strong components with periods of about 60 days, which are due to the aliased M_2 and S_2 tides. Comparing the periods of the dominant components in Figure 6 and the aliasing periods in Table 3, we believe that the T/P-derived SLAs over the Taiwan Strait and the East China Sea are affected by almost all aliased major ocean tides. As an example, we find that the Rms difference between CSR3.0 modeled and observed tidal values over 1993-1994 at the Taichung tide gauge station is 50 cm. The Taichung station is located on the central west coast of Taiwan, and there the tidal amplitude is 3 m. This explains why SLAs over the Taiwan Strait are so seriously affected by the aliased tides.

Wind has components with periods of 30-60 days [*Philander*, 1990], and in particular, the wind over the SCS has a component
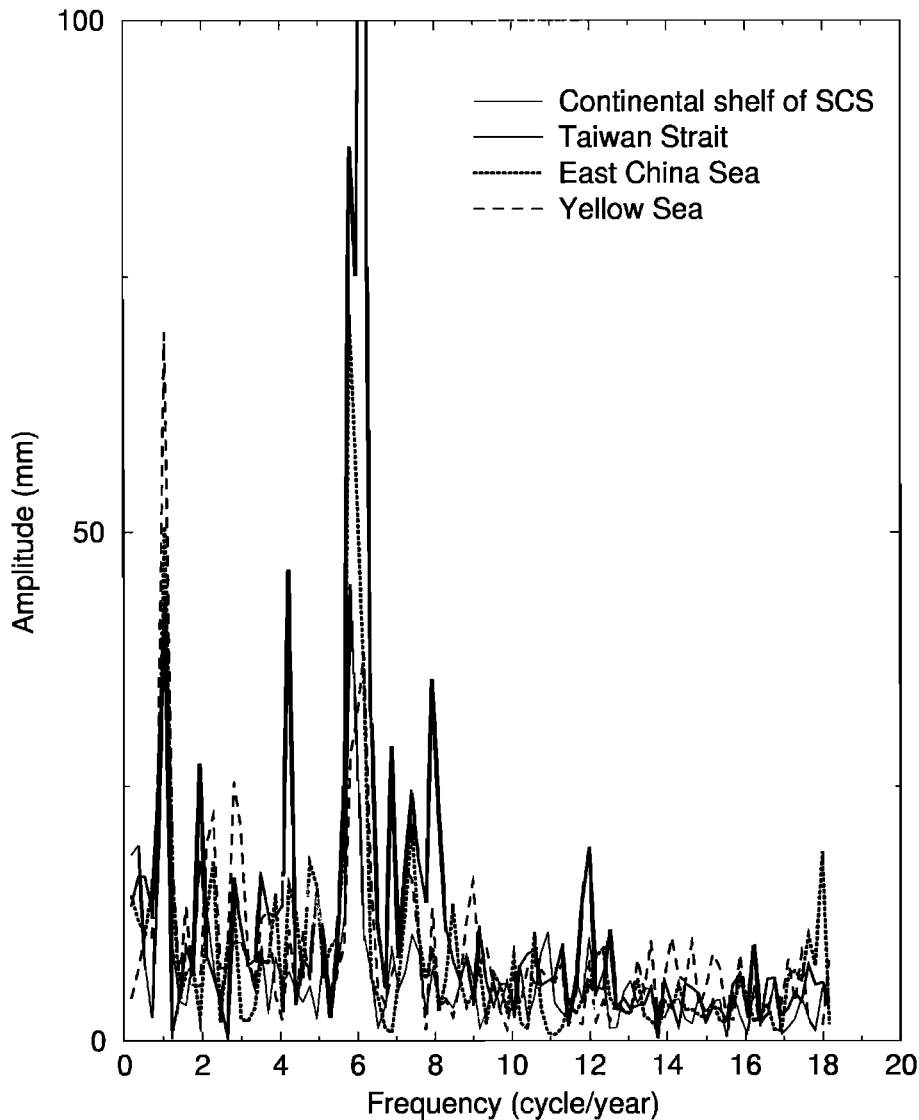
Figure 6. Comparison of periodograms of TOPEX/Poseidon-derived SLA in four areas of the continental shelf of east Asia.

with a period of 180 days due to the summer and winter monsoons (here we consider only the magnitude of wind; see below). All these wind components may give rise to sea level variability of the same frequencies. Because of the closeness between the periods of the wind components and the aliased periods of tides, there is considerable uncertainty as to whether certain components in the four SLA time series are due to aliased tides or are due to wind. However, if a component is due to an aliased tide, then this component should show consistent amplitude throughout the entire time span of a time series. To detect the time-variation of the amplitude of a component will rely on wavelet analysis discussed below. Moreover, to have less tidal aliasing effect and to have a time series that represents the overall behavior of the SCS sea level, only SLA3 will be used in the following analysis.

4. Wavelet Analysis of Sea Level Anomaly

In the Fourier analysis performed in Section 3.1, a time series is regarded as a stationary signal, so that in theory the spectral content of a segment of the series should be equivalent to that of any other segment. However, many signals, including SLA, are nonstationary and have time-varying frequencies and amplitudes. For example, sea level variabilities can be due to wind, sea surface temperature (SST), ENSO, and other forcings that have different magnitudes and frequencies at different times. To see the time-varying components of a signal, a better tool than Fourier analysis is wavelet analysis. In this study we employ both the continuous wavelet transform and the wavelet multiresolution transform to analyze SLA and other data. The continuous one-dimensional wavelet transform of a signal, $f(t)$, is defined as [Daubechies, 1992]

$$C(a,b) = \frac{1}{\sqrt{a}} \int f(t)\psi(\frac{t-b}{a})dt \quad , \tag{5}$$

where a and b are scale and translation, respectively, $\psi(t)$ is the wavelet function, and $C(a,b)$ is the wavelet coefficient. If ψ is a complex function, then we must use the conjugate of ψ in (5). Mathematically, $C(a,b)$ is the projection of $f(t)$ on $\psi((t-b)/a)$ or the inner product of $f(t)$ and $\psi((t-b)/a)$. The greater the similarity between $f(t)$ and $\psi((t-b)/a)$, the larger the coefficient $C(a,b)$. Thus large absolute values of the wavelet coefficients can

be easily used to identify the scale of the signal and its location on the t axis. The constant $1/\sqrt{a}$ in (5) is to ensure that the norm of $\psi((t-b)/a)$ is equal to the norm of $\psi(t)$, i.e., $\|\psi((t-b)/a)\| = \|\psi(t)\|$. The wavelet function $\psi(t)$ must have a compact support and satisfy the admissibility condition, which demands that the mean of $\psi(t)$ up to a certain order of moment be zero. Furthermore, small scale corresponds to high frequency and large scale corresponds to low frequency. Thus $C(a,b)$ represents the time-scale structure of a signal.

Since data are always given in a discrete form, the continuous wavelet transform is approximated as

$$C_{j,k} = \frac{1}{\sqrt{a_j}} \sum_{n=0}^{N-1} f(n\Delta t)\psi(\frac{n\Delta t - b_k}{a_j})\Delta t \quad , \tag{6}$$

where N is the number of records and Δt is the sampling interval. Equation (6) can be evaluated by algorithms such as fast Fourier transform [Torrence and Compo, 1998]. The discrete scales and translations are selected as

$$a_j = j\Delta t, j = 2,\cdots, J_{max}$$
$$b_k = k\Delta t, k = 0,\cdots, N-1 \quad , \tag{7}$$

where J_{max} is a number $<N$. The index j starts from 2 because $2\Delta t$ is the smallest resolvable scale. The choice of J_{max} depends on the spectral content of the analyzed signal, [see also Torrence and Compo, 1998; Kumar and Foufoula-Georgiou, 1994]. Note that Torrence and Compo [1998] and Kumar and Foufoula-Georgiou [1994] present two different criteria for choosing J_{max}.

Plate 1a shows the wavelet coefficients of SLA3 computed with the real part of the Morlet wavelet, defined as [Daubechies, 1992]

$$\psi(t) = \pi^{-1/4}e^{-t^2/2}\cos(5t) \quad , \tag{8}$$

The Morlet wavelet is widely used in geophysical research such as seismic data analysis. Properties of the Morlet wavelet in the time and frequency domains are given by Kumar and Foufoula-Georgiou [1994]. It is easy to show that the Morlet wavelet in (8) has a compact support and satisfies the admissibility condition up to any order of moment, see, for example, the

Table 4. Amplitudes and Phases of CSR3.0 Tide Model Errors at Three Tide Gauge Stations of the SCS

| Tide	Haikuo		Taiping		Dongsha	
	Amplitude, cm	Phase, deg	Amplitude, cm	Phase, deg	Amplitude, cm	Phase, deg
M_2	9.5	94.7	17.1	159.3	8.7	25 3
S_2	4.4	333.7	6.5	340.6	2.6	200.0
N_2	3.0	307.9	3.4	268.0	1.1	111.4
K_2	3.0	140.7	1 2	175.9	0.5	43.4
O_1	10.3	285.9	9.4	47 8	4.9	179.9
P_1	4.1	118.3	6.5	256.2	1.7	75.1
K_1	20.0	84.4	15.6	267.9	5.4	32.7
Q_1	1.5	29.5	1.8	152.2	0.3	281.8
Mm	1.7	237.4	0.3	6.2	3.9	256.4
Mf	1.2	314.3	0.9	321.9	0.6	317.7
Ssa	3.3	39.9	1.5	207.2	4.4	100.2

Signal
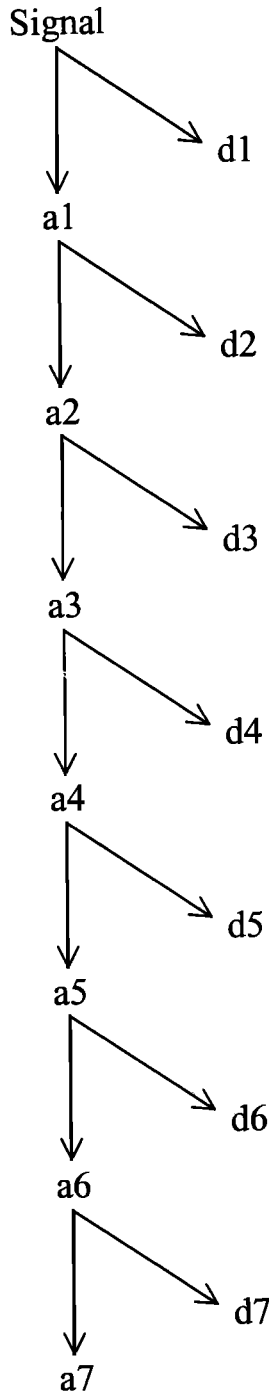
Figure 7. Wavelet decomposition tree of a seven level multi-resolution wavelet transform.

integration result by *Gradshteyn and Ryzhik* [1994, p. 531]. According to *Torrence and Compo* [1998, Table 1] the relationship between the period *p* (or wavelength) of a Fourier component and the scale *a* of the Morlet wavelet given in (8) is

$$p = \frac{4\pi a}{5+\sqrt{2+5^2}} = 1.232a \ , \tag{9}$$

which helps to interpret the wavelet coefficients in the Fourier sense. Furthermore, to reduce the edge effect in the wavelet transform, the data records were extended with zero values. Because of the edge effect, in a plot of wavelet coefficients there is

a zone called "cone of influence (COI)" [*Torrence and Compo,* 1998] where the coefficients are less reliable than those in other parts of the plot. However, according to *Torrence and Compo* [1998, p. 67], if the time series is cyclic, there will be no COI. Since the SLA time series (also the time series in Plates 1b and 1c) is dominated by the annual cycle (see Figure 5) and is almost cyclic, the COI of the wavelet coefficients in Plate 1 should be negligible. Below is a summary of the SLA components identified in Plate 1a.

1. The 30-120 day components are strong from January 1993 to January 1995 and weak after January 1995. The fact that these components have different amplitudes at different times suggests that SLA3 is not affected by the aliased M_2 and S_2 tides.

2. The semiannual component is identified as a local high in spring and a local high in winter in each year at period of 6 months. This component is due to the summer and winter monsoons of the SCS. The peaks always occur in May to June (for the spring high) and in November to December (for the winter high). In the springs of 1995 and in the winter of 1997-1998, such semiannual highs almost disappear. The time-varying amplitude of this component shows no contamination of aliased K_1 and Ssa tides in SLA3.

3. The annual component creates the almost periodic wavelet coefficients that can be easily identified in Plate 1a. It has a peak in summer, and the time span between two consecutive summer peaks is about 12 months. The amplitude varies from one year to another with the largest in 1996 and the smallest in 1994.

4. The wavelet coefficients corresponding to the interannual components are rather smooth. At periods of 2-3 years, two bands of highs occur between late 1993 and the summer of 1994 and between the summer of 1996 and the spring of 1997. Notice that the two bands of highs occur about 1 year before both the 1994-1995 and the 1997-1998 El Niños. At periods > 3 years, a band of highs begins in late 1995 and ends in the spring of 1997. In fact, the spring of 1997 is the time when the 1997-1998 El Niño starts to develop.

Next we perform wavelet multiresolution transform on SLA3. The multiresolution transform applies a wavelet matrix, consisting of scaling coefficients, to a data vector hierarchically to obtain a sequence of vectors containing approximations and details at different levels; see, for example, *Press et al.* [1993, p. 594] and *Chui* [1992, p. 20] for the computational algorithm. Thus, with the wavelet multiresolution transform, a signal is decomposed into components of different resolutions. For example, Figure 7 shows the wavelet decomposition tree of a seven-level decomposition of a signal. In Figure 7 we have the relationships $a_i = a_{i+1}+d_{i+1}$, and signal $= a_7+d_7+d_6+d_5+d_4+d_3+d_2+d_1$. The higher the degree of approximation, the lower the resolution. For example, a_2 is coarser than a_1. This is also true of the details. In this study we used the scaling coefficients of the Daubechies number 3 (db3) wavelet [*Daubechies,* 1992] to form the wavelet matrix for the multiresolution transform. The db3 wavelet has a compact support length of five, and up to the third order derivative of its Fourier transform at the origin (frequency = zero) is zero. Figure 8 shows a seven-level decomposition of SLA3, which is summarized as follows.

1. Detail d_1 detects five anomalously negative SLA values between January 1993 and January 1995. The responsible T/P cycles are 31, 41, 55, 65 and 79, when the Poseidon altimeter was on. It also shows that between January 1993 and January 1995, the monthly variability is much stronger than at any other time.

2. Approximations a_2 and a_3 show the seasonal variations of SLA. Detail d_3 shows the almost semiannual variation of sea level related to the summer and winter monsoons.

3. Approximation a_5 shows two local SLA maxima in January 1994 and in August 1996, which precede the 1994-1995 and the 1997-1998 El Niño and are closely linked to the local highs in the wavelet coefficients in Plate 1a.
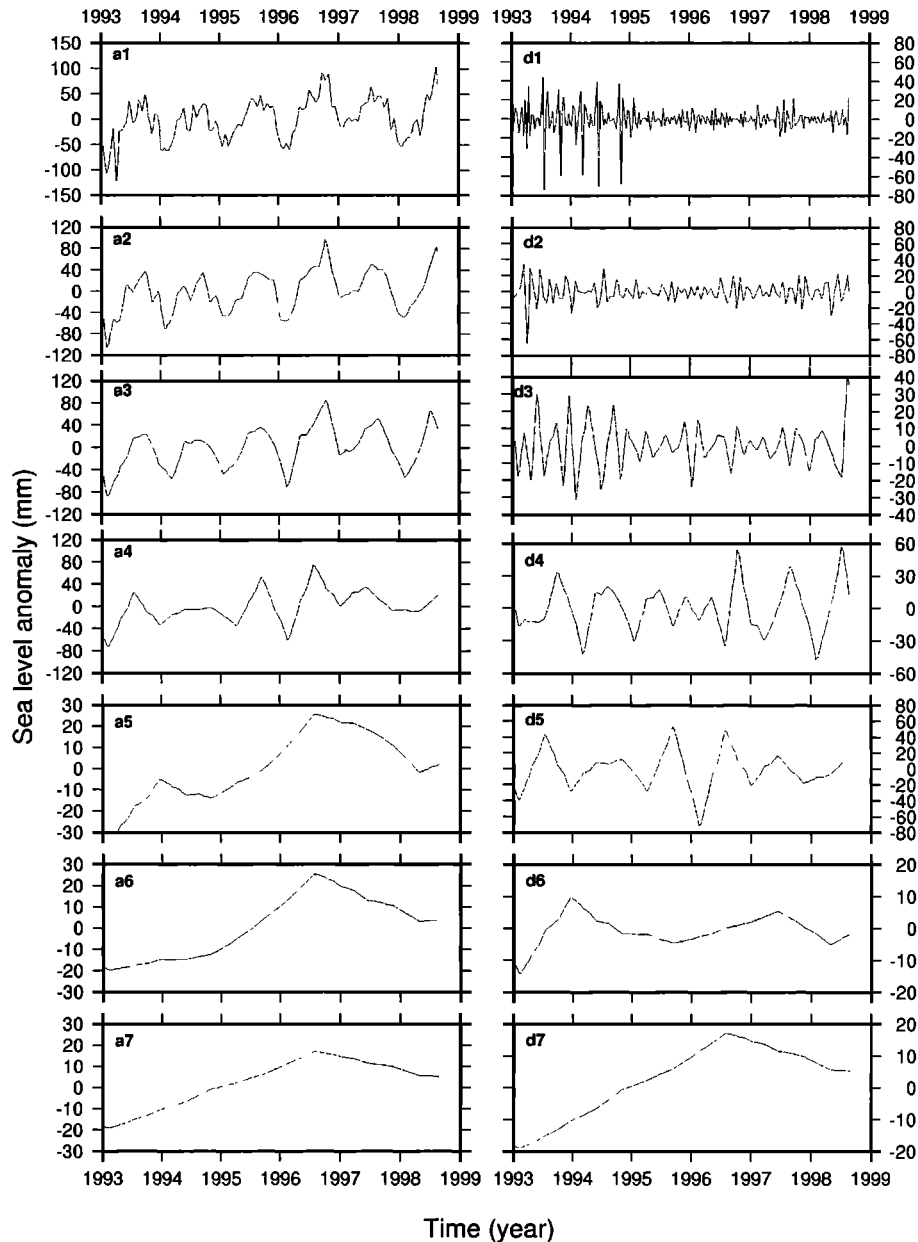
Figure 8. Approximations (a_1-a_7) and details (d_1-d_7) of sea level anomaly over the SCS from a seven-level multiresolution wavelet transform using the db3 wavelet.

4. Approximations a_6 and a_7 show the long-term trend of SLA. The sea level of the SCS increases from the beginning of the record in 1993, reaches a peak in the summer of 1996, and then falls off rapidly. On the basis of approximation a_7 a rising rate of 8.9 mm yr^{-1} is obtained. This regional rate over the SCS is considerably larger than the global rate of 2.1 mm yr^{-1} we obtain from T/P but agrees well with the regional results of *Nerem et al.* [1998] and *Cazenave et al.* [1998], and may be caused by the interdecadal climate variability in the North Pacific described by *Zhang et al.* [1997].

5. Relationships Among Sea Level, Wind and Temperature

5.1. Coherence and Frequency Response Functions

Many researchers, for example, *Shaw and Chao* [1994], *Shaw et al.* [1999], and *Wu et al.* [1998], have shown by dynamic

modeling or by empirical orthogonal function analysis that wind and temperature contribute to the variability of the SCS sea level. We now use Fourier and wavelet analyses to examine the spectral relationship of the sea level variability to these origins. First, we obtained weekly wind stress data from Centre ERS d'Archivage et de Traitement/France based on wind vectors measured by the scatterometers onboard ERS-1 and ERS-2 to derive the wind stress data [Maroni, 1995]. We also obtained weekly SST from Integrated Global Ocean Services System at the Columbia University, whose SST results are based on in situ data and the data from National Oceanic and Atmospheric Administration's advanced very high resolution radiometer [*Reynolds and Smith*, 1994]. The original wind stress and SST data are given on global 1°×1° grids. Subgrids over the SCS were then extracted from the global grids and used to form time-averaged grids. Wind stress anomaly (WSA) and sea surface temperature anomaly (STA) were then obtained by subtracting the respective time-averaged values from the original wind stress and the SST data. Because SLA3 contains some
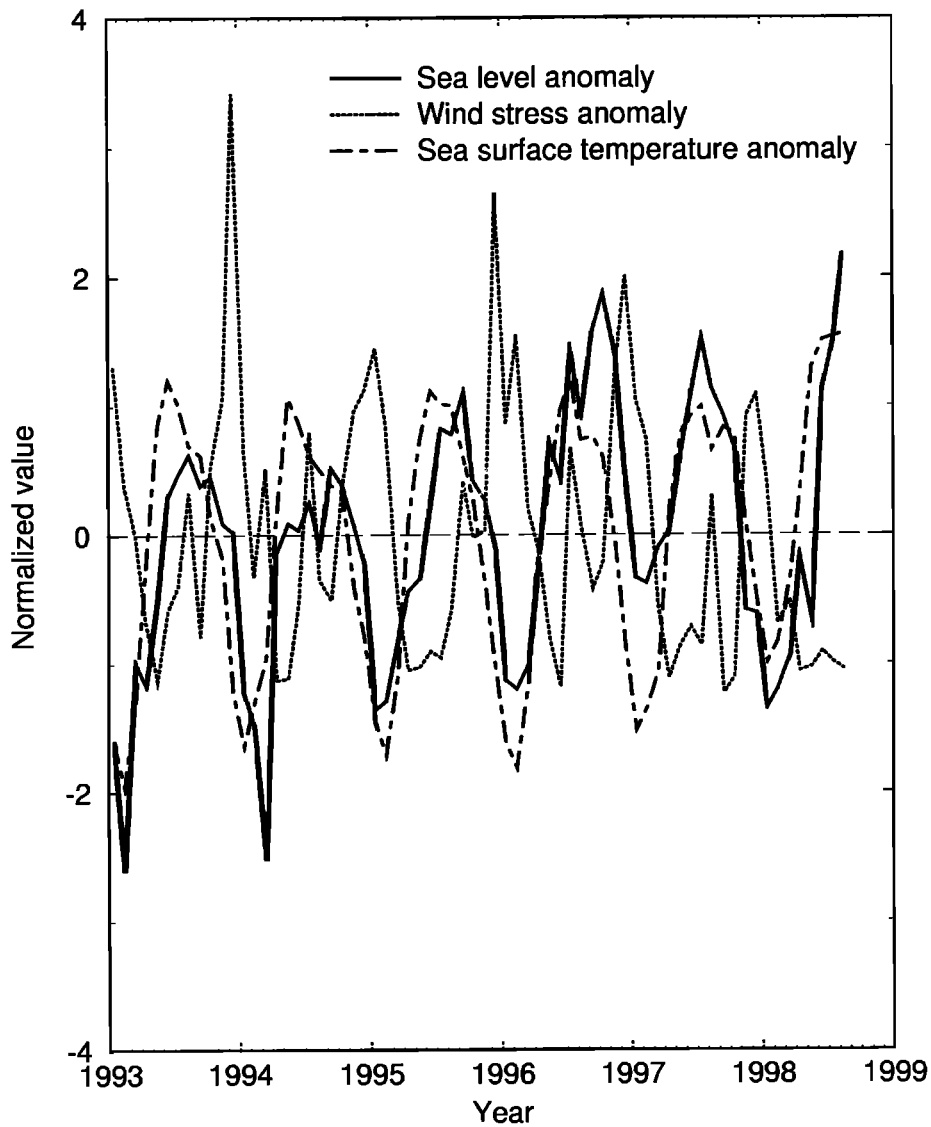
Figure 9. Normalized monthly SLA, WSA, and STA over the SCS.

anomalous values as found in detail d_1 and the weekly WSA and STA over the SCS are very noisy, we applied a Gaussian filter with a wavelength of 1 month to SLA, WSA, and STA to obtain smooth monthly time series for further investigations. To compare different signals in the time and frequency domains, we normalized the signals as

$$z_p = \frac{p - \bar{p}}{\sigma_p} \ , \tag{10}$$

where $\bar{p}$ and σ_p are the mean and the standard deviation of signal p, respectively. The means of SLA, WSA, and STA are 2.8 mm, 0.0002 Pa (1 Pa = 1 N m^{-2}), and -0.05°C, respectively and their standard deviations are 39.8 mm, 0.03 Pa, and 1.5°C , respectively. Figures 9 and 10 show the normalized SLA, WSA, and STA and their periodograms. The three signals are dominated by the annual component. For SLA and STA the annual peaks occur in summer, but for WSA the annual peaks occur in winter because of the winter monsoon. However, on average the SLA peaks are 27 days behind the STA peaks. The WSA peaks always occur in December and on average are 68 days ahead of the SLA lows and 41 days ahead of the STA lows. Because of the 1 month

sampling interval, we cannot see any components with periods <60 days. WSA also has strong components with periods of 413, 188, 103, and 159 days (in the order of decreasing amplitude). The amplitudes of STA at frequencies higher than 2 cycles yr^{-1} are relatively small compared to those of SLA and WSA.

To quantify the relationship between the three anomaly time series, we compute the coherence function defined as

$$\gamma^2_{xy}(f) = \frac{\left|G_{xy}(f)\right|^2}{G_{xx}(f)G_{yy}(f)} \ , \tag{11}$$

where f is frequency, G_{xy} is the cross spectrum between x and y, and G_{xx} and G_{yy} are the autospectra of x and y, respectively. The coherence function $\gamma^2_{xy}(f)$ falls into the interval [0,1] and represents the correlation of two variables at frequency f. It is a much better tool than the statistical correlation coefficient function. A reliable method for estimating autospectra and cross spectra is the ensemble averaging method in which the data sequence is divided into several segments and the estimated autospectra and cross spectra are the averaged spectra from these segments [*Bendat and Piersol*, 1993; *Press et al.*, 1993]. Welch's tapering function
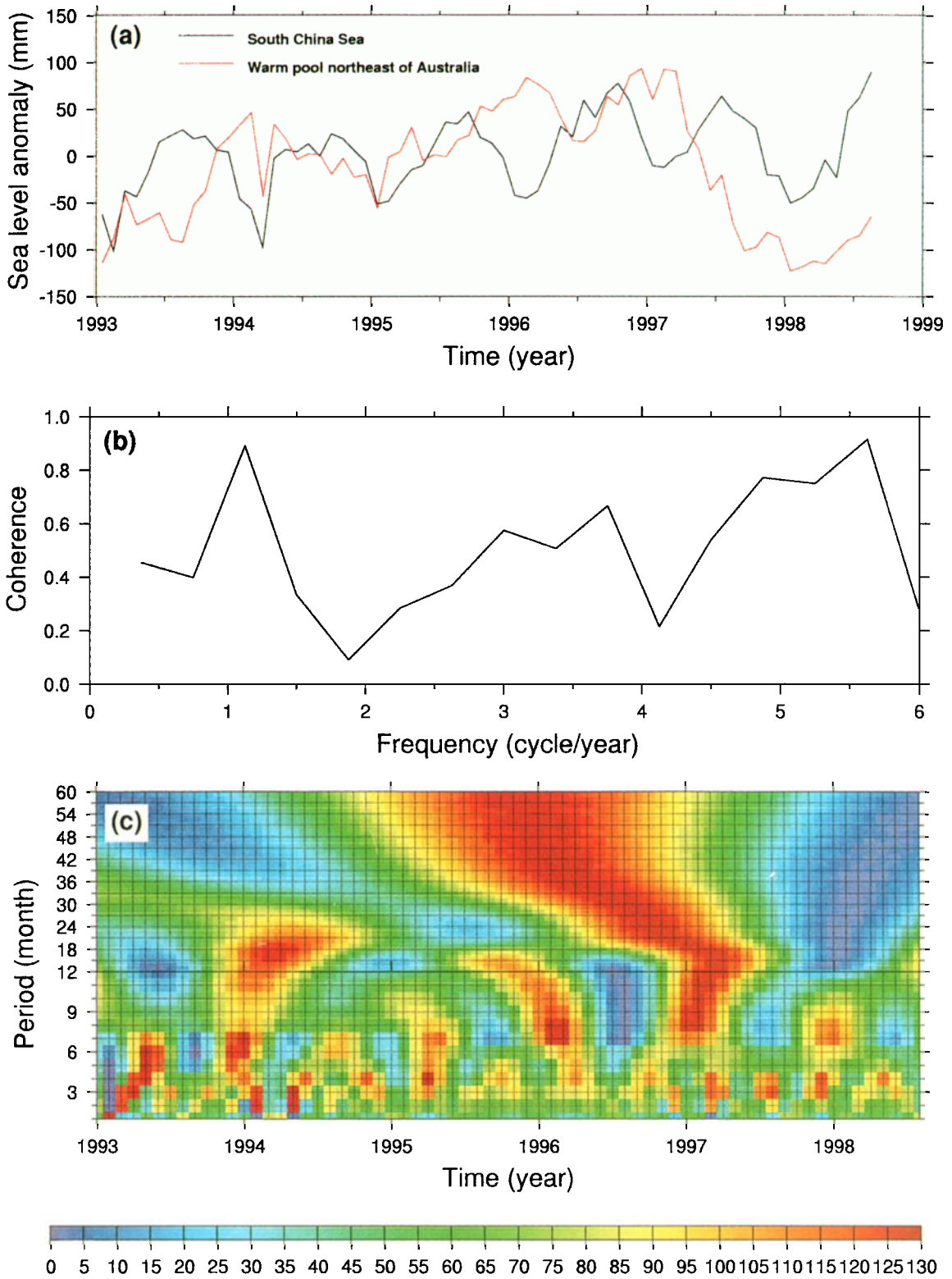
Plate 3. (a) Time series of the SLA over the SCS and over the warm pool northeast of Australia, (b) the coherence between the two time series, and (c) the wavelet coefficients of SLAWP.
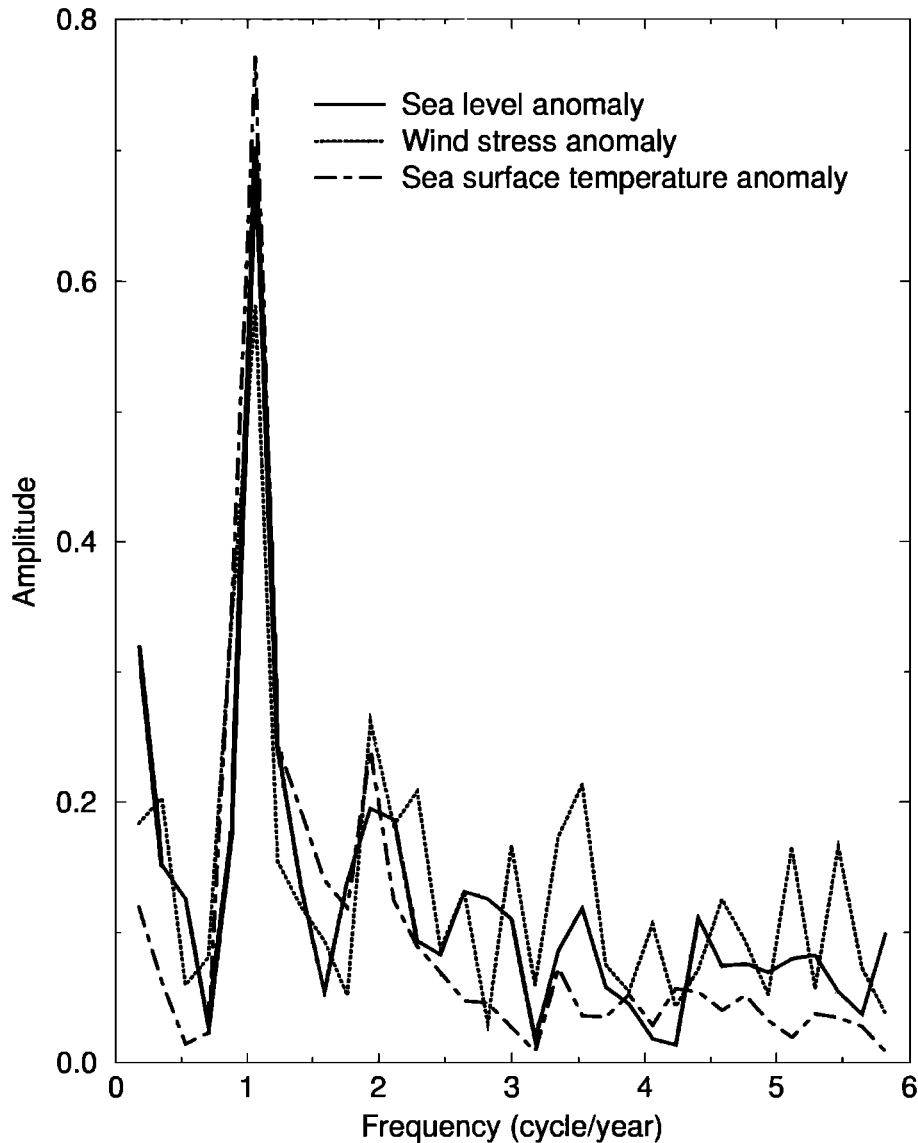
Figure 10. Periodograms of normalized SLA, WSA, and STA over the SCS.

[*Press et al.*, 1993, p. 547] was used to avoid side lobes in the spectra. Because the monthly data are relatively short, only two segments were used in the ensemble averages. Although this will result in relatively large errors in the estimated spectra, we can obtain a maximum frequency resolution, which is 0.375 cycle yr^{-1} in this case. Figure 11 shows the coherence functions of WSA-SLA, STA-SLA, and WSA-STA. At frequencies around 1 cycle yr^{-1}, the three pairs have the largest coherences. The fact that the coherences at one cycle yr^{-1} exceed 0.9 suggests that the annual components of SLA, WSA, and STA may all arise from the same source. At frequencies around 2 and 4 cycles yr^{-1}, both WSA-SLA and STA-SLA have the second largest coherences, but here the signal-to-noise ratios are nearly one because the coherences are around 0.5. At frequencies around 2 and 6 cycles yr^{-1}, the coherences of WSA-STA are nearly 0.9, which is relatively large compared to the coherences of WSA-SLA and of STA-SLA. At the other frequencies there are no significant correlations in the three pairs. In addition, for both WSA-SLA and STA-SLA the lowest coherences occur at frequencies around 3 cycles yr^{-1}. A coherence <1 indicates that there is noise in the input and the output or that the relationship between the input and the output is nonlinear or

both. The larger the noise or the larger the degree of nonlinearity, the smaller the coherence. Moreover, if the output is due to inputs besides the input under consideration, the coherence will be <1.
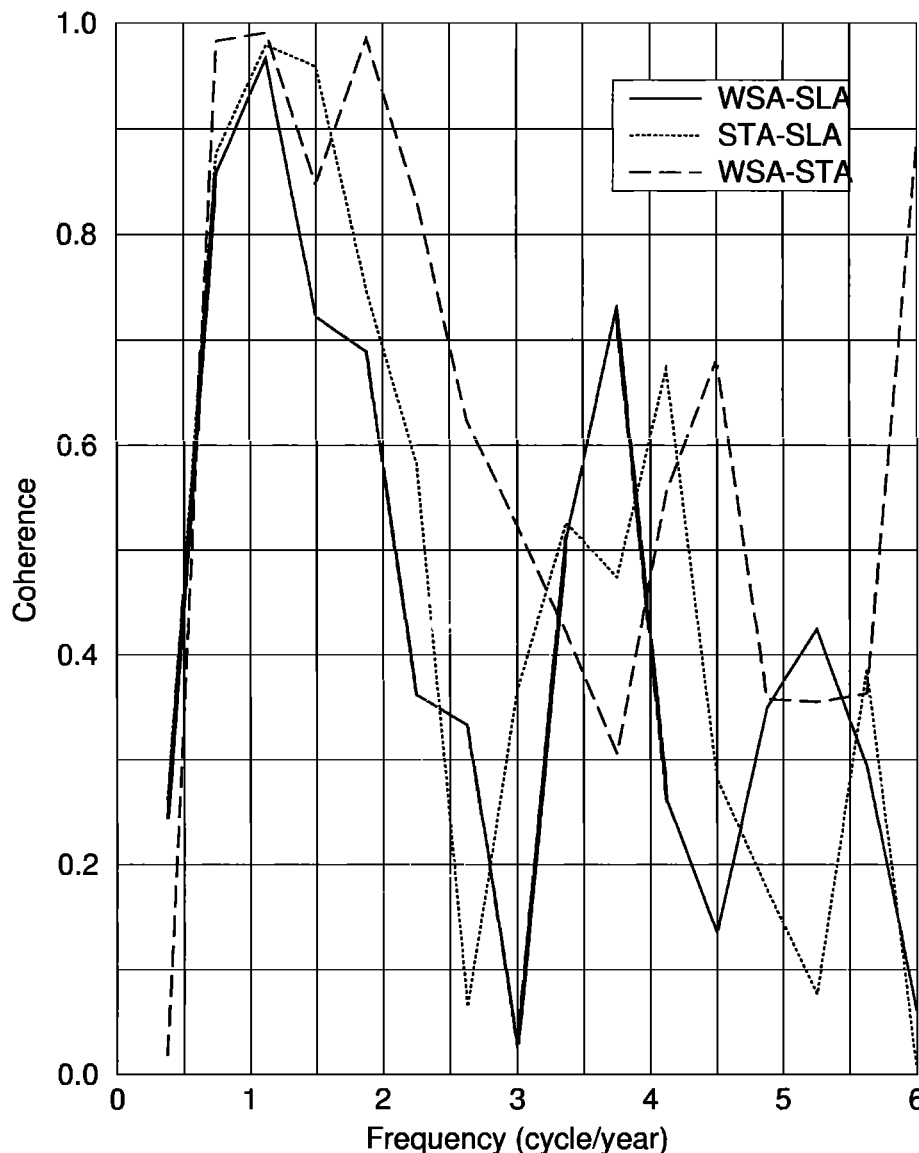
If the WSA-SLA, STA-SLA, and WSA-STA relationships are linear, we have

$$Y(f) = H(f)X(f) \ ,\tag{12}$$

where X is the Fourier transform of the input (x), Y is the Fourier transform of the output (y), and H is the frequency response function. In a pair such as WSA-SLA the first item (WSA) is the input, and the second one (SLA) is the output. The frequency response function can be estimated as

$$H(f) = \frac{G_{xy}(f)}{G_{xx}(f)} = |H(f)|e^{-i\phi(f)} \ ,\tag{13}$$

where $|H(f)|$ is the gain and $\phi(f)$ is the phase at frequency f. If $\phi(f)$ is positive, then at frequency f, x leads y by $\phi(f)/2\pi f$ in time ($\phi(f)$ is in radian). Note that the simple linear

Figure 11. Coherences between WSA and SLA (WSA-SLA), between STA and SLA (STA-SLA), and between WSA and STA (WSA-STA).

relationship in (12) by no means represents the actual complex interaction among sea level, wind, and temperature; it merely helps to explain gain and phase. Figure 12 shows the gains and phases of the response functions for the three pairs. At frequencies between 0.375 and 2.625 cycles yr^{-1}, the three pairs have the same pattern of gain, and in this frequency band WSA-SLA and STA-SLA have the largest gains at the lowest frequency of 0.375 cycle yr^{-1}. Beyond 2.625 cycles yr^{-1}, the gains of WSA-SLA and WSA-STA fall off sharply. Beyond 1.875 cycles yr^{-1}, the response function of STA-SLA behaves like a downward continuation operator [*Meskó*, 1984], which enhances the high-frequency components of SLA, except at 6 cycles yr^{-1} where the gain drops to a relatively low value of 0.3. The negative phases in WSA-SLA and WSA-STA and the positive phases in STA-SLA before 2.25 cycles yr^{-1} are consistent with the phases of the annual and the semiannual components of the times series shown in Figure 9. The phase of zero at 6 cycles yr^{-1} in WSA-STA means that at this frequency STA responds to WSA immediately without a phase lag, while the phase of 180° at 6 cycles yr^{-1} in WSA-SLA and STA-SLA

indicates that at this frequency SLA responds to WSA and STA with a phase lag of 1 month. If we consider only the gains at 1 cycle yr^{-1}, the SCS sea level responds to wind stress at a rate of 1.34 m Pa^{-1} and to SST at a rate of 23 mm $°C^{-1}$.

5.2. Comparison of Wavelet Coefficients

To compare the wavelet coefficients of WSA and STA with those of SLA, we resampled the weekly WSA and STA into two time series using a data interval of 9.9156 days. The wavelet coefficients of WSA and STA were then computed using the Morlet wavelet and are shown in Plates 1b and 1c. Below is a summary of the comparison of the three sets of wavelet coefficients.

1. The 30-60 day components of SLA, WSA, and STA all have time-varying magnitudes. The wavelet coefficients of the three signals do not always have the same order of magnitude at the same time, suggesting that at these periods SLA does not always respond to wind or temperature in the same way.
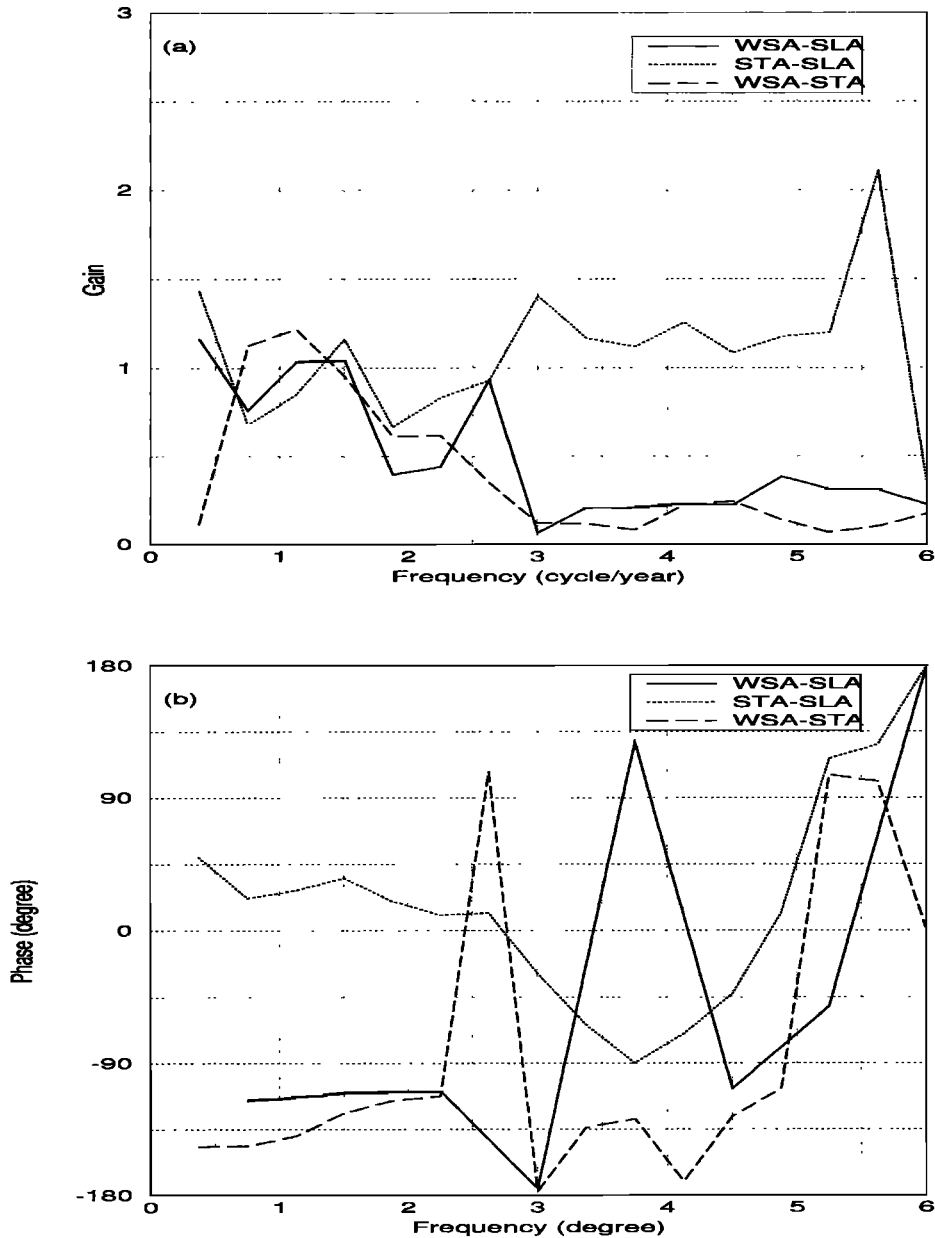
Figure 12. (a) Gains and (b) phases of the response functions in the WSA-SLA, STA-SLA, and WSA-STA relationships.

2. All the three signals have the semiannual component because of the summer and winter monsoons. For this component the phase of SLA is almost equal to that of STA but is different from that of WSA. Like SLA, WSA is also weak in the summer after an El Niño.

3. All the three signals are dominated by the annual component. While the peaks of the annual components of SLA and STA are in summer, the peak of the annual component of WSA is in winter. All the three signals have amplitudes that vary from one year to another. Note that in the winters of 1992-1993 and 1997-1998, WSA is particularly weak. In the cold La Niña year of 1996, both SLA and WSA are strong. In general, the annual SLA and WSA components are weak in the years of El Niño, except in 1994-1995. This phenomenon agrees with the observation by Gu and Philander [1995].

4. At periods of 1-2 years, SLA is similar to STA, and both have local highs in the summers of 1993, 1995, and 1996. At

periods of 2-5 years, SLA is similar to WSA, but the WSA pattern clearly leads SLA by a few months, and the STA pattern follows SLA. Both SLA and WSA have local highs in 1993-1994 and 1996-1997, just prior to the 1994-1995 and 1997-1998 El Niños. At periods above 3 years, STA has local highs in 1994-1995 and in 1997-1998. The local high of STA in 1997-1998 seems to be very unusual. In fact, the rising trend of STA still exists in the winter of 1998-1999 and has significantly disrupted local weathers in the western Pacific.

6. Onset Date of Summer Monsoon and SLA Zero Crossing

Xie et al. [1998] computed the onset dates of the summer monsoon of the SCS from 1979 to 1995 and showed that the onset dates have interannual variability. We notice that in SLA3, shown in Figure 2, the sea level of the SCS begins to rise in March and

Table 5. Dates of the SLA Zero Crossing and the Onset of Summer Monsoon

	1993	1994	1995	1996	1997	1998
Zero Crossing	June 4	April 28	May 26	April 28	May 1	May 28
Monsoon	June 4	May 4	June 2	NA[a]	NA[a]	NA[a]

[a]NA, not available.

reaches a peak in September. At some point in spring, SLA becomes positive. In Table 5 we list the dates of these SLA zero crossings in spring, as well as the onset dates of the summer monsoons of the SCS obtained from *Xie et al.* [1998]. Remarkably, the two sets of dates agree very well for 1993, 1994, and 1995. In particular, in the years after El Niños, namely, 1993, 1995, and 1998, the dates of SLA zero crossings are in late May or early June, while in the "regular" years, the dates of SLA zero crossings are in late April or early May, which agree with the average onset date of May 4 from *Xie et al.* [1998]. The reason for the SLA zero crossing could be that after an El Niño the easterly trade wind becomes strong in the western Pacific. This strengthening then

delays the development of the southwesterly wind, which carries warm air from the tropic to the SCS. Since SLA and STA are positively correlated at the seasonal time scale, the SLA zero crossing will be delayed as well. Figure 13 shows the west-east and north-south components of the wind speed over the SCS. After the 1994-1995 and 1997-1998 El Niños the westerly winds in the springs of 1995 and 1998 are relatively weak. Furthermore, in the springs of 1995 and 1998 the west-east components are smaller than the north-south components. In the regular years the two wind components have almost the same magnitude and sign, indicating that the summer and winter monsoons must blow in the northeast-southwest direction. Although there are only three
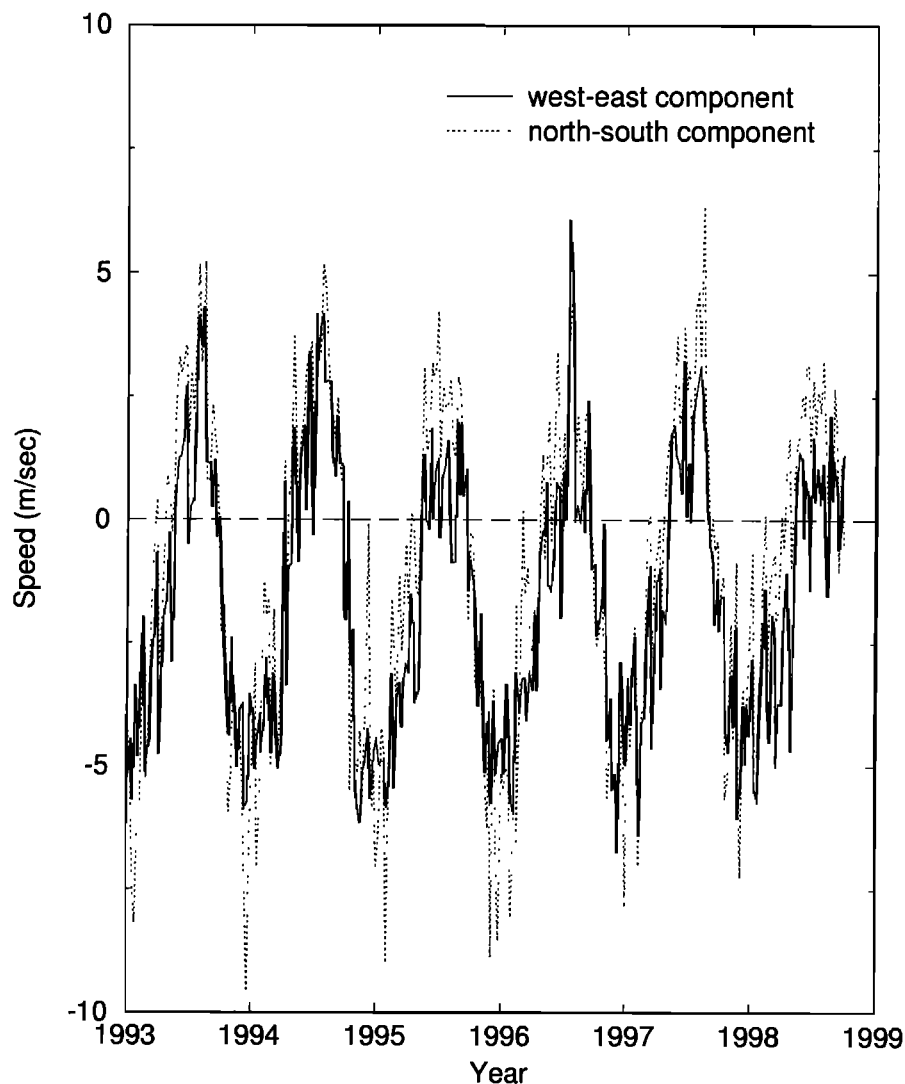
Figure 13. West-east (positive to the east) and north-south (positive to the north) components of the wind speed over the SCS.

instances here, it may be hypothesized that the SLA zero crossing in spring can be a precursor to the onset of the summer monsoon. If this hypothesis is true and is to be put into operational use, we will need nearly real-time T/P altimeter data to calculate the date of the SLA zero crossing over the SCS. Nearly real-time T/P altimeter data with precise orbits are possible because of the use of Global Positioning System for orbit determination [*Lichten et al.*, 1996]. More study is needed to see if the onset of summer monsoon and the SLA zero-crossing are the result of the air and the sea over the SCS responding to a common forcing in spring and their respective response functions having the same phase.

7. Relationship Between Sea Level Anomaly and ENSO

Much has been said in Sections 4 and 5 about the relationship between the sea level of the SCS and ENSO. Here we wish to quantify this relationship. We obtain the monthly time series of NINO3 SST (actually, it is the difference between the recorded and the normal SST), which is defined as the area-averaged SST over the region $5°S - 5°N, 150° - 90°W$ and is widely used as an index of ENSO. Wavelet analysis of ENSO is given by, for example, *Wang and Wang* [1996] and *Torrence and Compo* [1998]. Plate 2a shows the wavelet coefficients of NINO3 SST. According to *Kiladis and Diaz* [1989], after 1980, El Niños have occurred in 1982-1983, 1987-1988, 1992-1993, 1994-1995, and 1997-1998, and La Niñas have occurred in 1989 and 1996. Thus, from 1980 to 1999, El Ninos occurred every 2-5 years, while La Niñas occurred less frequently. In Plate 2a, the occurrences of El Niño/La Niña are identified as highs and lows of wavelet coefficients at the interannual timescales. In order to see the relationship between the SCS sea level and ENSO for a longer time than just 5.6 years, the monthly SLAs at the Zhapo tide gauge station recorded from 1980 to 1993 were added to SLA3 to form a time series covering 1980-1999. Zhapo is located in the northern SCS, and its location is shown in Figure 1. Plate 2b shows the wavelet coefficients of this extended SLA time series. In Plate 2b it appears that there is no discontinuity at the connecting point of 1993-1994. It must be pointed out that the SLA values at Zhapo are only point values, rather than area-averaged values as in SLA3, which is considered a representative SLA time series of the whole SCS. From the wavelet coefficients in Plates 2a and 2b, we find a rule (except in 1990): An El Niño starts to develop when the El Niño-like wavelet coefficients of the SCS change curvature from negative to positive.

The El Niño-like wavelet coefficients are defined as the wavelet coefficients at periods of 2-5 years that have a local high as compared to the neighboring coefficients. For example, at periods of 30 months, from the autumn of 1996 onward the SLA wavelet coefficients start to increase, then reach a peak in the early 1997, and finally, change curvature from negative to positive in the summer of 1997, and exactly from this time on, the 1997-1998 El Niño starts to develop. The exception in 1990 may be due to fact that sea level at one tide station cannot fully represent the SCS sea level. In Plates 2a and 2b, we also mark the locations where the El Niño-like wavelet coefficients change curvature from negative to positive. This interesting relationship can be explained by the development of the warm pool northeast of Australia preceding an El Niño. The seawater over this warm pool is piled up over time, and at some point the water is released and travels as a Kelvin wave to the eastern tropic Pacific, resulting in an El Niño. Geographically, the SCS is close to this warm pool whose sea level should be correlated with that of the SCS. To see the degree of their correlation, we computed a monthly T/P SLA time series (warm pool SLA (SLAWP)) over the area $17°S - 3°N, 150 - 170°E$, roughly covering the warm pool. Plate 3

shows the comparison of the monthly SLA3 and SLAWP time series, their coherences, and the wavelet coefficients of SLAWP. At frequencies of 1.125 and 5.625 cycles yr⁻¹, SLA3 and SLAWP have coherences of 0.90, thus the annual and the 60 day components of the SCS SLA are highly correlated with the same components of the warm pool SLA. At interannual timescales the pattern of SLA3 is similar to that of SLAWP. However, at periods above 3 years the SLAWP pattern leads SLA3. The wavelet coefficients of both time series have local highs in 1993-1994 and in 1996-1997 (see also approximation a_5 in Figure 8). As stated before, these two local highs occurred just prior to the 1994-1995 and 1997-1998 El Niños. Also, both sets of wavelet coefficients have local lows after about September 1997.

From the above analysis the El Nino-like wavelet coefficients of SLAWP or SLA3 may be useful in predicting El Niños. Of course, in the predictions the wavelet coefficients must be aided by additional data such as the Southern Oscillation Index or even seismic data [*Walker*, 1999]. The recommended procedure is first to obtain nearly real-time T/P SLA over the warm pool or the SCS via the Internet. The SLA is fed to a wavelet analysis program to get an updated plot of wavelet coefficients like the one in Plate 1a (the total record length must be at least 5 years). The plot of wavelet coefficients can be placed on an independent page at a World Wide Web site where other relevant information for El Niño also exists. If the El Niño-like wavelet coefficients in the plot change curvature from negative to positive, which typically happens in spring or summer, then an El Niño will be likely to develop.

8. Conclusions

This study uses Fourier and wavelet analyses to examine the T/P SLA time series over the SCS and its relationships to wind, SST, and ENSO. Fourier analysis gives the overall characteristics of the signals under study in the frequency domain, while wavelet analysis shows the time-frequency spectra of the signals. Altimeter data, even as precise as those from T/P, must be used with cautions. Probably the most damaging effect to SLA comes from tidal aliasing, which can yield false components of sea level variability. The T/P record length of 5.6 years used in this study is too short to see the interdecadal variability of the SCS sea level. However, with many ongoing altimeter missions such as T/P, Geosat-Follow-On, and ERS-2 and future missions such as JASON-1 and Envisat-1 a long record of SLA purely from altimetry can be expected. Important conclusions in this study are (1) that the annual component of SLA is highly correlated with the annual components of wind and SST and the semiannual component of SLA is generated largely by the summer and winter monsoons and that both the annual and semiannual components have time-varying amplitudes, (2) that the SLA of the SCS has interannual components with periods of 2-5 years, whose phases are about 1 year ahead of El Niño, (3) that the SLA zero crossing date in spring is almost coincident with the onset date of the summer monsoon, and (4) that the El Niño-like wavelet coefficients may be useful in predicting El Niños.

References

Archiving, Validation, and Interpretation of Satellite Oceanographic Data (AVISO), *AVISO User Handbook for Merged TOPEX/Poseidon Products*, third ed., 1996.

Bendat, J. S., and A. G. Piersol, *Engineering Applications of Correlation and Spectral Analysis*, 2nd ed., John Wiley, New York, 1993.

Cazenave, A., K. Dominh, C. Brossier, M. C. Gennero, P. Bonnefond, F. Barlier, and P Exertier, Mean sea level investigation at global and regional scales from TOPEX/Poseidon, *AVISO Altimetry Newsl.*, *6*, 23-24, 1998.

Chui, C. K., *An Introduction to Wavelets*, Academic, San Diego, Calif., 1992.

Daubechies, I., *Ten Lectures on Wavelets*, Soc. for Ind. and Appl. Math., Philadelphia, Pa., 1992.

Eanes, R., and S. Bettadpur, *The CSR 3.0 Global Ocean Tide Model*, Cent. for Space Res., Univ. of Tex., Austin, 1995.

Foufoula-Georgiou, E., and P. Kumar (Eds.), *Wavelets in Geophysics*, Academic, San Diego, Calif., 1994.

Fu, L.-L., E. J. Christensen, C. A. Yamarone Jr., M. Lefebvre, Y. Menard, M. Dorrer, and P. Escudier, TOPEX/Poseidon mission overview, *J. Geophys. Res.*, *99*, 24,369-24,382, 1994.

Gradshteyn, I. S., and I. M. Ryzhik, *Table of Integrals, Series, and Products*, 5th ed., Academic, San Diego Calif., 1994.

Gu, D., and S. G. H. Philander, Secular changes of annual and interannual variability in the tropics during the past century, *J. Clim.*, *8*, 864-876, 1995.

Hu, J. -H., Study on surface currents in the South China Sea, paper presented at Workshop of Oceanography, Hsinchu, Taiwan, NSC, 1998.

Hwang, C., and S. -A. Chen, Circulations and eddies over the South China Sea derived from TOPEX/Poseidon altimetry, *J. Geophys. Res.*, in press, 2000.

Kiladis, G. N., and H. F. Diaz, Global climatic anomalies associated with extremes in the Southern Oscillation, *J. Clim.*, *2*, 1069-1090, 1989.

Kumar, P., and E. Foufoula-Georgiou, Wavelet analysis in geophysics: an introduction, *Wavelets in Geophysics*, edited by E. Foufoula-Georgiou and P. Kumar, pp. 1-44, Academic, San Diego, Calif., 1994.

Lau, W. K. -M., South China Sea monsoon experiment observed from satellites, *Eos Trans., AGU, 78, p. 599*, 1997.

Lemoine, F. G., et al., The Development of the Joint NASA GSFC and the National Imagery and Mapping Agency (NIMA) Geopotential Model EGM96, *NASA Tech. Pap., NASA/TP-1998-206861*, 575 pp., 1998.

Lichten. S. M., B. J. Haines, R. J. Muellerschoen, Y. Vigue, and T. Munson, Rapid service precise orbit determination capability from GPS for altimetry missions, *Eos Trans. AGU*, 77(46), Fall Meet. Suppl., F129, 1996.

Maroni, C., The quarterly topic: Offline wind field production, *CERSAT News*, *5*, 2-3, 1995.

Meskó, A., *Digital Filtering: Applications in Geophysical Exploration for Oil*, Pitman, London, 1984.

Nerem, R. S., G. T. Mitchum, and B. S. Giese, An investigation of very low frequency sea level change using TOPEX/Poseidon, *AVISO Altimetry Newsl.*, *6*, 88-89, 1998.

Parke, M. E., R. H. Stewart, D. L. Farless, and D. E. Cartwright, On the Choice of orbits for altimetric satellite to study ocean circulation and tides, *J. Geophys. Res.*, *92*, 11,693-11,707, 1987.

Philander, S. G., *El Niño, La Niña, and the Southern Oscillation*, Academic, San Diego, Calif., 1990.

Pope, A. J., The Statistics of Residuals and the Detection of Outliers, *Tech. Rep. NOS65 NGS1*, Rockville, Md., 1976.

Press, W. H., S. A. Teukolsky, B. P. Flannery, and W. T. Vetterling, *Numerical Recipes*, 2nd ed., Cambridge Univ. Press, New York, 1993.

Reynolds, R. W., and T. M. Smith, Improved global sea surface temperature analyses, *J. Clim.*, *7*, 929-948, 1994.

Schlax, M. G., and D. B. Chelton, Aliased tidal errors in TOPEX/Poseidon sea surface height data, *J. Geophys. Res.*, *99*, 24,761-24,775, 1994.

Shaw, P.-T., and S.-Y. Chao, Surface circulation in the South China Sea, *Deep Sea Res., Part I, 41*, 1663-1683, 1994.

Shaw, P.-T., S.-Y. Chao, and L.-L. Fu, Surface height variations in the South China Sea from satellite altimetry, *Oceanol. Acta, 22*, 1-17, 1999.

Tapley, B. D., et al., The Joint Gravity Model 3, *J Geophys. Res., 101*, 28,029-28,049, 1996.

Torrence, C., and G. Compo, A practical guide to wavelet analysis, *Bull. Am. Meteorol. Soc., 79*, 61-78, 1998.

Walker, D. A., Seismic predictors of El Niño revisited, *Eos Trans. AGU, 80*, p. 281, 1999.

Wang, B., and Y. Wang, Temporal structure of the Southern Oscillation as revealed by waveform and wavelet analysis, *J. Clim.*, 9, 1586-1598, 1996.

Wessel, P., and W. H. F. Smith, New version of the Generic Mapping Tool released, *Eos Trans. AGU, 76*, p. 329, 1995.

Wu, C.-R., P.-T. Shaw, and S. -Y. Chao, Seasonal and interannual variations in the velocity field of the South China Sea, *J. Oceangr., 54*, 361-372, 1998.

Xie, A., Y. -S. Chung, X. Liu, and Q. Ye, The interannual variations of the summer monsoon onset over the South China Sea, *Theor. Appl. Climatol., 59*, 201-213, 1998.

Zhang, Y., J. M. Wallace, and D. Battisti, ENSO-like interdecadal variability: 1900-93, *J. Clim., 10*, 1004-1020, 1997.

S.-A. Chen and C. Hwang, Department of Civil Engineering, National Chiao Tung University, 1001 Ta Hsueh Road, Hsinchu 300, Taiwan. (hwang@geodesy.cv.nctu.edu.tw)